REPORT DOCUMENTATION PAGE	*Form Approved* *OMB No. 0704-0188*

The public reporting burden for this collection of information is estimated to average 1 hour per response, including the time for reviewing instructions, searching existing data sources, gathering and maintaining the data needed, and completing and reviewing the collection of information. Send comments regarding this burden estimate or any other aspect of this collection of information, including suggestions for reducing the burden, to the Department of Defense, Executive Service Directorate (0704-0188). Respondents should be aware that notwithstanding any other provision of law, no person shall be subject to any penalty for failing to comply with a collection of information if it does not display a currently valid OMB control number.

PLEASE DO NOT RETURN YOUR FORM TO THE ABOVE ORGANIZATION.

1. REPORT DATE (DD-MM-YYYY) 2708/2007	2. REPORT TYPE FINAL	3. DATES COVERED (From - To) 9/2/2002-9/2/2006

4. TITLE AND SUBTITLE Discrimination, Identification and Tracking of Unresolved Targets Using Tomographic Integration of Multiplex Sensor Data	5a. CONTRACT NUMBER
	5b. GRANT NUMBER F49620-02-1-0335
	5c. PROGRAM ELEMENT NUMBER
6. AUTHOR(S) Dr. David Brady	5d. PROJECT NUMBER
	5e. TASK NUMBER
	5f. WORK UNIT NUMBER

7. PERFORMING ORGANIZATION NAME(S) AND ADDRESS(ES) Duke University Office of Research Support Box 90077 Durham, NC 27708	8. PERFORMING ORGANIZATION REPORT NUMBER

9. SPONSORING/MONITORING AGENCY NAME(S) AND ADDRESS(ES) AFOSR, Dr. Kent Miller /NE 801 N. Randolph Street St Suite 732 Arlington, VA 22203-1977	10. SPONSOR/MONITOR'S ACRONYM(S) AFOSR
	11. SPONSOR/MONITOR'S REPORT AFRL-SR-AR-TR-07-0362

12. DISTRIBUTION/AVAILABILITY STATEMENT
Approved for public release; distribution unlimited.

13. SUPPLEMENTARY NOTES
The views, opinions and/or findings contained in this report are those of the author(s) and should not be construed as an official Department of the Air Force position, policy or decision, unless so designated by other documentation.

14. ABSTRACT
This final report describes progress in the 2002-2006 fiscal years in development of a small aperture telescope array for identification and tracking of flying objects using their visible spectral radiance and position.
The goal of this project is to simultaneously track and identify objects in orbit. Here we describe several instruments we have developed based on spectrally dispersive elements rather than interferometric designs. These systems also capture spatial and spectral information from a target point source, but do not exhibit the multiplex disadvantage in SNR. These systems concentrate the signal photons onto one or a few narrow bands on the detector, rather than the RSI, which distributes the signal photons across the entire detector. These dispersive systems are also less sensitive to vibration and precise alignment versus the RSI system.

15. SUBJECT TERMS
Tracking, shear interferometer

16. SECURITY CLASSIFICATION OF:			17. LIMITATION OF ABSTRACT	18. NUMBER OF PAGES	19a. NAME OF RESPONSIBLE PERSON D. Brady
a. REPORT	b. ABSTRACT	c. THIS PAGE			
UNCLASSI	UNCLASSI	UNCLASSI	UL		19b. TELEPHONE NUMBER (Include area code) 919-660-5394

Standard Form 298 (Rev. 8/98)
Prescribed by ANSI Std. Z39.18
Adobe Professional 7.0

20070925386

' 2. Objective:

The goal of this project is to develop small aperture spatio-spectral sensors for space and projectile tracking. The project began as an extension on interferometric techniques developed over the past decade, but we have recently discovered novel dispersive techniques that we expect to yield major improvements.

3. Status
The program has been completed and will be described in this final report.

4. Accomplishments/New Findings: See attached Final Report
    A. Spatio-spectral Tracking with a Rotational Shear Interferometer
    B. Dispersive Instruments for Spatio-spectral Point Source Tracking
    C. Dispersion Multiplexing Spectrometer
    D. Remote Raman Spectrometers
    E. High-throughput Hyperspectral Microscopy

5. Personnel Supported: The following individuals have worked on this topic during the program's execution:

David J. Brady Robert
Guenther Evan Cull
Michael Gehm
And Evan Cull has received his PhD.

6. Publications: Papers published during the reporting period:
1. Shawn Kraut, Jason Gallicchio and David Brady, "Estimation with rotational shear interferometric sensor arrays," SPIE annual meeting

2. Bristol Crawford, "Rotational shear interferometery for astronomical imaging," senior thesis, Physics Department, Duke University

3. "Standoff raman spectroscopy system for remote chemical detection",
      E.C. Cull, M.E. Gehm, B.D. Guenther, and D.J. Brady, SPIE, Boston Dec 2005.

4. "High-throughput Hyperspectral Microscopy", M.E. Gehm and D.J. Brady, SPIE, 2005.

5. Standoff raman spectroscopy system for remote chemical detection. E.C. Cull, M.E. Gehm, B.D. Guenther, and D.J. Brady Duke University Fitzpatrick Center for Photonics and Communications Systems, Durham, NC 27708

6. Evan Cull, "Computational Spectroscopy for Task Specific Sensing" PhD thesis, Department of Electrical and Computer Engineering, Duke University.

7. Interactions/Transitions: Have begun a program with the **Edgewood Chemical Biological Center** [W91ZLK-07-P-1536]entitled **"Development of a Coded Aperture Spectrometer for Ultraviolet Raman"**

8. New discoveries, inventions, or patent disclosures: The following patents are in process: US. Patent Application No.11/391,223 filed March 29, 2006.

A. Spatio-spectral Tracking with a Rotational Shear Interferometer

A.1 Background

Spatio-spectral tracking with the rotational shear interferometer (RSI) involves both spatial and spectral interferometric sensing. It is useful to describe a couple of simpler examples before addressing the RSI. The next two sections will discuss the Fourier transform spectrometer (interferometric spectral sensing) and the use of the RSI as a monochromatic coherence imager (interferometric spatial sensing).

A.1.1 Fourier Transform Spectroscopy

As stated in the introduction, the Fourier transform spectrometer was first introduced when Michelson developed the interferometer which bears his name. Many varieties of the Fourier transform spectrometer exist, but all operate by interfering the input field with a time delayed version of itself.[†] An example of a Michelson interferometer is shown in Fig. 2.1 with input field U. The interferometer is composed of a beamsplitter and two mirrors. Upon entering the interferometer the input field, U, is split and traverses the two arms of the interferometer. The mirrors reflect the divided field, and the beamsplitter recombines the fields, directing half to the detector and the other half out the input aperture. If the field from the arm with Mirror 1 is $U(t)$ then the field from the other arm is $U(t + \tau)$ where τ is the delay introduced in the

[†]A non-interferometric Fourier transform spectrometer exists, known as the Mertz Mock Interferometer. The mock interferometer is a unique case and is not relevant in a discussion of the RSI. [7]
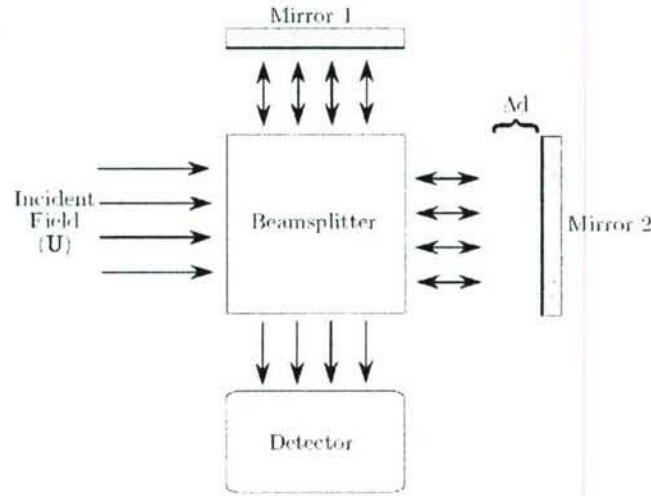
Figure 2.1: Diagram of a Michelson Interferometer with input field U and path length difference of Δd.

field by the path length difference of Δd:

$$\tau = \frac{2\Delta d}{c} \qquad (A.1)$$

where c is the speed of light. Optical detectors measure intensity rather than the amplitude and phase of the field. The time averaged intensity of the field U is represented as:

$$I_0 = \langle |U|^2 \rangle \quad (A.2)$$

where the $\langle U \rangle$ represents an ensemble average over U. The interferometer's detector measures

the intensity of the sum of the field reflected from each of the arms of the interferometer. The

detected intensity is a function of the path length difference:

$$
\begin{aligned}
I(\tau) &= \langle |U(t)U(t+\tau)|^2 \rangle \\
&= \langle U(t) + U(t+\tau) \rangle + \langle U^*(t)U(t+\tau) \rangle + \langle U(t)U^*(t+\tau) \rangle \quad (A.3) \\
&= 2I_0 + 2\mathcal{R}e\{G(\tau)\}
\end{aligned}
$$

The function $G(\tau)$ is the autocorrelation function, defined as:

$$G(\tau) = \langle U^*(\tau)U(t+\tau) \rangle . \quad (A.4)$$

The Wiener-Khinchin theorem states that the autocorrelation of a signal and its power spectral

density are related by the Fourier transform:

$$G(\tau) = \int_0^\infty S(v)\exp(j2\pi v\tau)dv , \quad (A.5)$$

where $S(v)$ is the power spectral density. [8] Since the power spectral density of signal is real, and its integral over all frequencies is equivalent to the measured intensity of the signal:

$$\int_0^\infty S(v)dv = I_0, (A.6)$$

it is possible to relate the intensity detected by the Michelson interferometer over a range of τ to the power spectral density. Starting with Eq. A.3 and substituting Eq. A.6 for $I0$ and Eq. A.5 for $G(\tau)$ yields:

$$I(\tau) = 2\int_0^\infty S(v)dv + 2\mathcal{R}e\left\{\int_0^\infty S(v)\exp(j2\pi v\tau)dv\right\}$$
$$= 2\int_0^\infty S(v)dv + 2\int_0^\infty S(v)\cos(2\pi v\tau)dv \qquad (A.7)$$

Solving for the intensity at $\tau = 0$ yields:

$$I(0) = 4\int_0^\infty S(v)dv, (A.8)$$

which can be combined with Eq. A.7 to produce: 1

$$I(\tau) - \frac{1}{2}I(0) = 2\int_0^\infty S(v)\cos(2\pi v\tau)dv. (A.9)$$
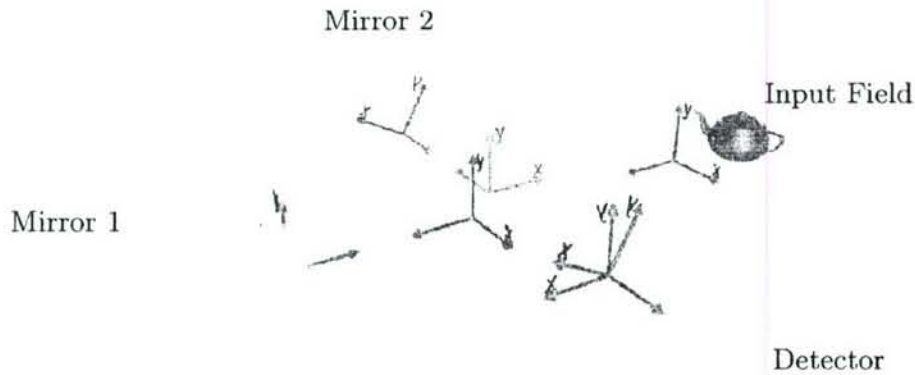

Figure 2.2: Diagram of a rotational shear interferometer.

This is a cosine Fourier relationship between the intensity detected as a function of τ and the power spectral density, which can be solved for power spectral density:

$$S(v) = \int_0^\infty 2[I(\tau) - I(0)]\cos(2\pi v\tau)d\tau \ . \ (A.10)$$

The Fourier transform relation between spectrum and intensity described by Eq. A.10 show that all measurements over τ contribute to each frequency, v, in the spectrum. Since the instrument is sampling in the Fourier space of the spectrum, a greater range covered in Fourier space (the range of τ) equates to recording more detailed spectral information, yielding a higher resolution measurement.

A.1.2 Rotational Shear Interferometer

The rotational shear interferometer (RSI) is similar to a Michelson interferometer except that the planar mirrors on the arms are replaced by right-angle folding mirrors. Fig. 2.2 shows a diagram of an RSI. The RSI allows us to measure the mutual coherence of the incident wavefront by interfering the wavefront with a rotated and time-delayed version of itself. One of the arms of the RSI can be rotated about the optical path, producing the shearing angle. A wavefront incident upon the RSI is initially split by the beam splitter and then traverses both of the arms. One of the arms folds the wavefront (labeled Mirror 1 in Fig. 2.2) while the other both folds and rotates the wavefront (labeled Mirror 2 in Fig. 2.2). The arm with the rotation mechanism is also translatable, allowing for a path length difference between the two arms, just like the Michelson interferometer. After traversing the arms, the wavefront is recombined and imaged on a digital focal plane.

The RSI used in this project was designed at the University of Illinois at Urbana-Champaign, and the components manufactured by the electrical engineering departmental machine shop. Like most interferometers, the RSI is sensitive to vibrations and mechanical disturbances on the order of a single wavelength of light. For this reason, the RSI was built from Invar, a metal alloy with a very low coeffcient of thermal expansion around room temperatures. The beam splitter and folding-mirrors used the design are one-inch optics. Since the RSI was designed for use in the visible region of the electromagnetic spectrum, the optics all have anti-reflective coatings to minimize losses at the air-glass interfaces. Figure 2.3 shows a photograph of the RSI.

2.1.3 The RSI in Astronomy

The RSI has been used in astronomy, primarily during the 1970s and 1980s before adaptive optics became available to the astronomy community. All uses of the RSI during this period applied the Van Cittert-Zernike theorem. [9] This theorem states that under the restriction of a quasi-monochromatic spectrum, a measurement of mutual intensity from a source is equivalent to the Fourier transform of the spatial intensity distribution of the source. This allows astronomers to reconstruct the image of a star from the FFT of the interference pattern recorded with an RSI from a telescope and narrow band spectral filter. Initially, Breckenridge analyzed an interferometer identical to an RSI with the shear fixed at 90 degrees. [10] His goal was to take high resolution astronomical images through the atmosphere. He collected a set of short exposure interference patterns, eliminated the interference patterns that were distorted by atmospheric turbulence, and combined the remainder for analysis. Later, the RSI was used and analyzed by

Roddier, Mariotti, and Chelli for successful stellar observations. [11–14] In all cases, photon efficiency was a serious problem because of the narrow band spectral filters used to meet the quasi-monochromatic source condition. A more recently proposed use for the RSI in astronomy is as a nulling interferometer for extrasolar planet detection. [15] Since the RSI has a null response for a point source directly on the optical axis, this paper suggests that extrasolar planets could be detected by pointing the optical system directly at a star and looking at the result.
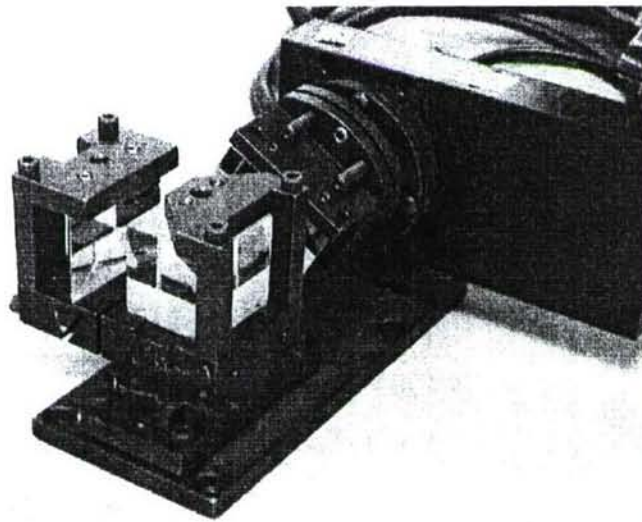
Figure 2.3: Photograph of the rotational shear interferometer.

A.2 Spatio-spectral Tracking of Orbiting Objects

Conventional systems for satellite tracking and identification involve imaging the satellite's structure using a large aperture telescope and adaptive optics. These telescopes are somewhat rare and quite expensive, so more recent methods attempt to identify the satellite by recording its spectral profile as it crosses from horizon to horizon. This typically involves the use of a spectrometer coupled to a telescope that is aimed at the satellite using a separate guiding system. The spectral profile of the satellite is measured in the visible wavelength range, measuring the spectrum of sunlight reflected from the satellite. This project uses a rotational shear interferometer (RSI) coupled to a telescope to simultaneously collect spatial tracking information and spectral reflectance information from the target satellite.

A.2.1 Conventional Systems

Conventional systems used for satellite tracking and identification can be separated into two

categories. Instruments in the first category capture an image of a satellite's structure for identification purposes. Not many of these systems exist since they require a multi-meter aperture, a fast and stable mount, and adaptive optics. One such system is the Maui Space Surveillance System (MSSS) run by the Air Force, based on a 3.67 m telescope. One project attaches a hyperspectral imager to the MSSS to capture spatial and spectral information. [16] It uses a set of tuneable spectral filters which are scanned over a period of time to create a hyperspectral image of the target.

The second category of systems used to track and identify satellites involves non-resolved object characterization. These systems image the satellite as a point source, using a telescope of diameter 500 mm or less. Tracking is easily accomplished by locating the point source in the field of view of the telescope. Satellite identification with these smaller systems is performed via four color photometry. This procedure measures the intensity of the observed point source through four different spectral filters. These filters are known as BVRI filters, corresponding to blue, green, red, and infrared. These four intensity values are then matched to a spectral database to find a close match for the satellite in question. Multiple BVRI intensity values can be recorded for a satellite as it crosses the sky, collecting a spectral reflectance profile for different sides of the satellite. Much of the research in this area involves algorithms to match the BVRI filter data to a database built from computer-modeled reflectance data. [17, 18]

A.2.2 Tracking with a Rotational Shear Interferometer

The target of interest for RSI tracking is a non-resolvable object in orbit. This means that a combination of the object's physical dimensions, its distance from the observer, and atmospheric turbulence causes the object to appear as a point source. Since the point source is in the far field, the field at the RSI can be approximated as a plane wave. The intensity response of an RSI to a monochromatic plane wave input is:

$$I_{detected} = 1 + \cos\left\{\frac{4\pi\sin(2\theta)}{\lambda}\tan(\phi_y)x\right\} \quad (A.11)$$

In Eq. A.11, θ is the shear angle of the RSI's rotating arm, λ is the wavelength of the source, and ϕ_y is the angle between the source and the optical axis of the interferometer. Figure 2.4 shows the angle ϕ_y and the coordinate system for the interferometer.

For a monochromatic point source and with a fixed shear angle, the RSI records a cosine fringe pattern whose frequency depends on both the wavelength of the source and the angle between the source and the optical axis. The rotation angle of the fringes on the detector plane (about the optical axis) depends on the elevation and azimuthal directions to the target (ϕ_x, ϕ_y).

This relation is shown in Fig. 2.5. If both the wavelength and the location of the point source are unknown, two measurements must be made from different perspectives (essentially for two different values of ϕ_y to spatio-spectrally locate the source.
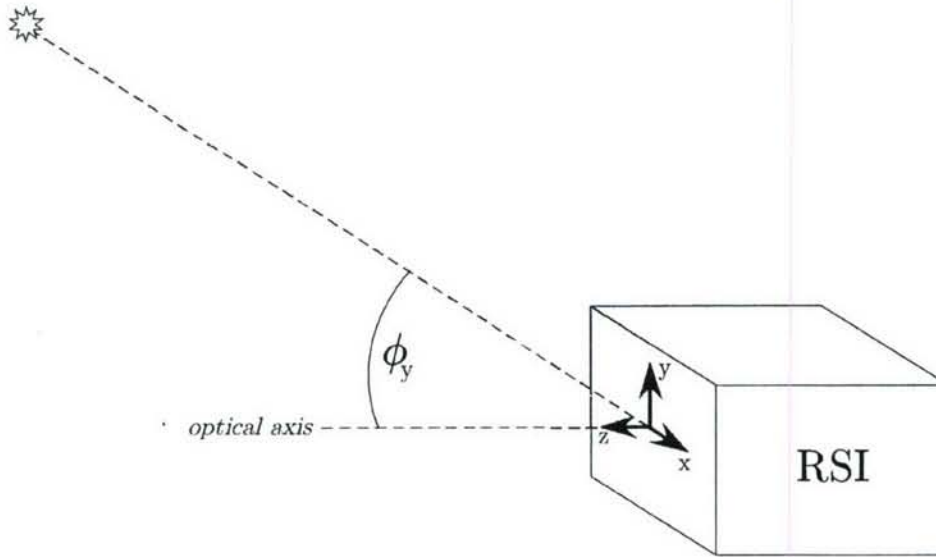

Figure 2.4: Diagram showing RSI, target, and coordinate axis.

A non-monochromatic source can be treated as a linear combination of monochromatic sources of different wavelengths. The visibility of the fringe pattern decreases as more spectral components are added, the result of the decrease in coherence length for a spectrally broader source. A simulated fringe pattern for a non-monochromatic source located at $(\phi_x, \phi_y) = (0.2, 0.2)$ radians is shown in Fig. 2.6.

As discussed in the overview of Fourier transform spectroscopy, the Wiener-Khinchin theorem relates fringe intensity for a range of different path-length delays (τ) to the power spectral density of the source. With a nonzero shear angle, a single RSI measurement fringe intensities for a range of τ because of the path-length difference between the rotated and fixed mirrors. A two-dimensional FFT of the RSI's source.
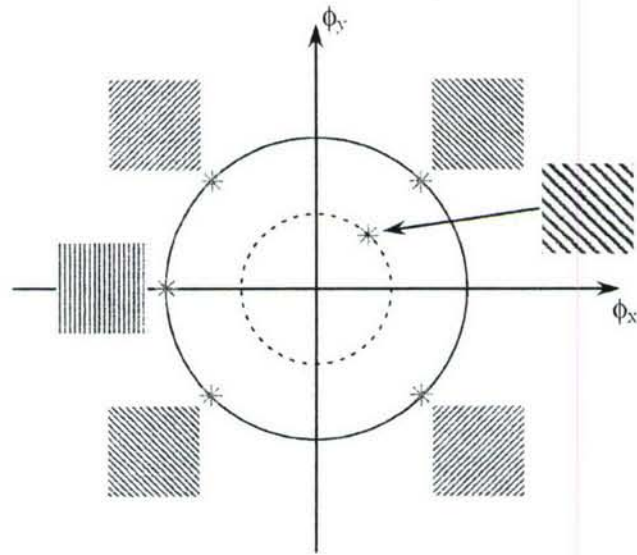
Figure 2.5: RSI fringe orientation based on target displacement from optical axis .
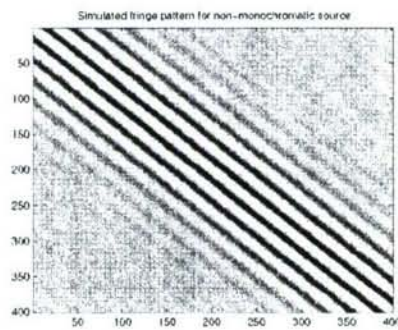

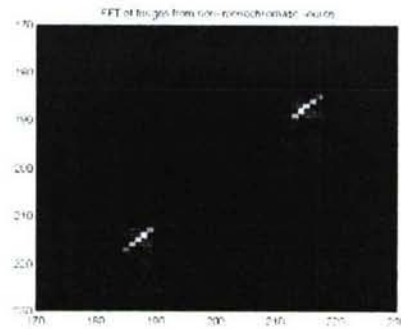Figure 2.6: Simulated RSI fringes for a non-monochromatic point source.

Figure 2.7: FFT of the fringe pattern created by the non-monochromatic point
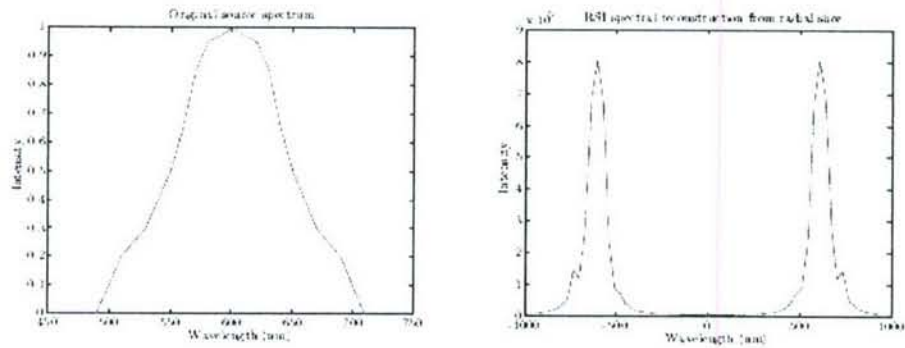

Figure 2.8: Original source spectrum and spectral estimate from simulated fringes.

fringe pattern yields spectral data along a radial line in the resulting image, as shown in Fig. 2.7. A cross section of the FFT image along the radial line produces a spectral estimate of the source, appearing in Fig. 2.8. The angle between the radial line and the "axes" of the image, as well as the distance from the center of the image to the spectral content, both relate to the spatial position of the source. Similar to the monochromatic case, two measurements must be recorded from different perspectives to determine the position of the source and properly scaled spectral information.
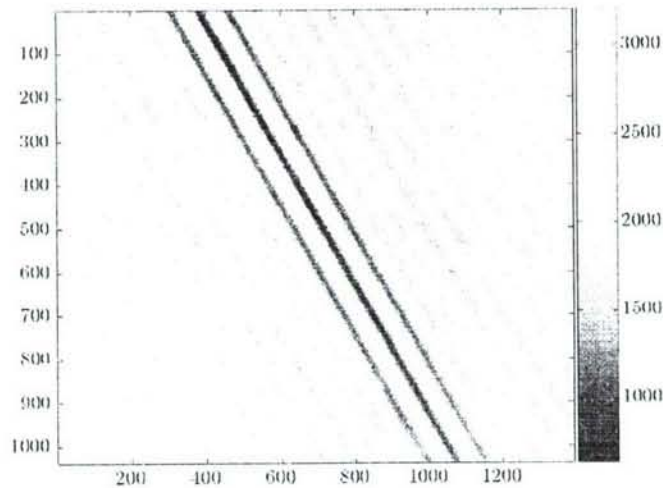
Figure 2.9: RSI fringes for a white LED.

A.3 Experimental Data

A.3.1 RSI Measurement of a White LED

After constructing and aligning the RSI shown in Fig. 2.3, a white LED was used to demonstrate the system performance. The LED was approximately 1 mm in size and was placed 1.5 m downrange from the RSI so that it approximated a point source. The fringe pattern for the white LED is recorded in Fig. 2.9. The pattern is not centered because the camera was not on the optical axis of the interferometer. Fortunately, sufficient fringe information was recorded to further process the data. The FFT of the fringes and a radial cross section showing the spectral data are shown in Fig. 2.10. There is a large low frequency component to the information in Fig. 2.9, so a small region in the center of the FFT was manually set to zero. This removes some of the low frequency noise from spectral data, making the LED spectrum more visible. The spectral reconstruction from the RSI data is compared to a spectrum of
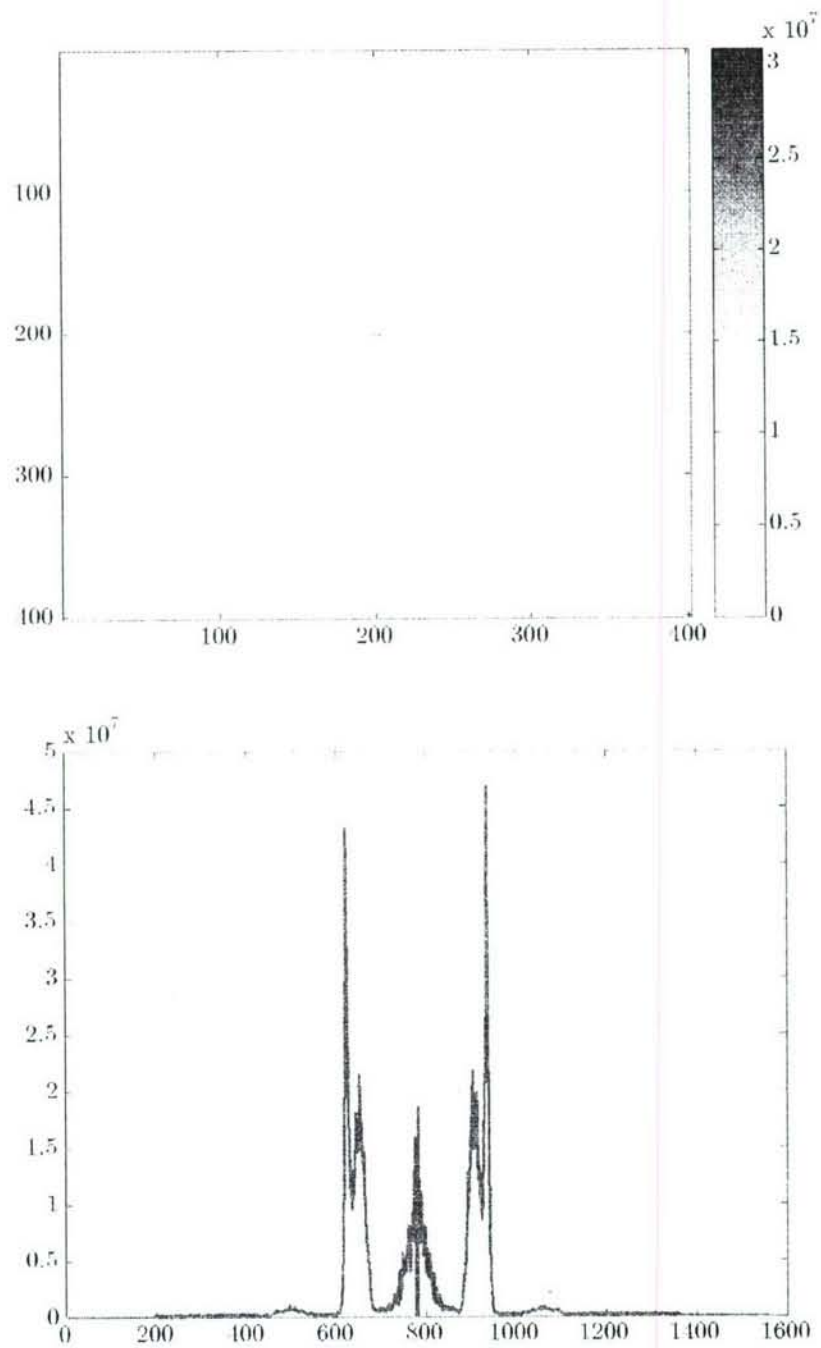
Figure 2.10: FFT of white LED fringes (top) and radial cross section showing spectral data (bottom).

the white LED measured by an Ocean Optics spectrometer in Fig. 2.11.

'A.3.2 RSI Measurement of Polaris

Attaching the RSI to a telescope increases the light input to the RSI, allowing the system to image dim objects like stars and satellites. The RSI / telescope system is a pupil imaging system where an image of the aperture of the telescope is formed through the RSI onto a focal plane. After initial work at the Three College Observatory (TCO) in Greensboro, NC, it seemed advantageous to use a telescope with a clear aperture. The telescope at the TCO is a Richey-Chretien model, using a secondary mirror in the aperture. The secondary mirror creates an obstruction in the middle of the measured interference pattern, as seen in Fig. 2.12. Upon testing an RSI attached to a small (102 mm) refracting telescope, shown in Fig. 2.13, it was determined that the light gathering ability of available refracting telescopes was not suffcient. (Reflecting telescopes are much cheaper than refracting telescopes for apertures over 100 mm.) For better light gathering, the current telescope system uses a 254 mm Schmidt Cassegrain telescope made by Meade. The beam leaving the telescope is folded into a vertical path by a dielectric mirror and then collimated by an achromatic doublet lens. The collimated beam is folded again so that it is directed into the an RSI, mounted on top of the telescope tube. Figure 2.14 shows a diagram of this system beside a picture of the telescope with RSI attached.

Different stars were used as the target points sources instead of orbiting satellites. Stars are easier targets to track because they are brighter and move much more slowly than visible satellites. (Geosynchronous satellites are, of course, stationary in the sky, but their high orbit makes them practically invisible.) The example data presented here are measurements taken of Vega. Vega is a very bright star, of magnitude 0.03. The RSI and telescope system recorded the fringes shown in Fig. 2.15 for a 30 second
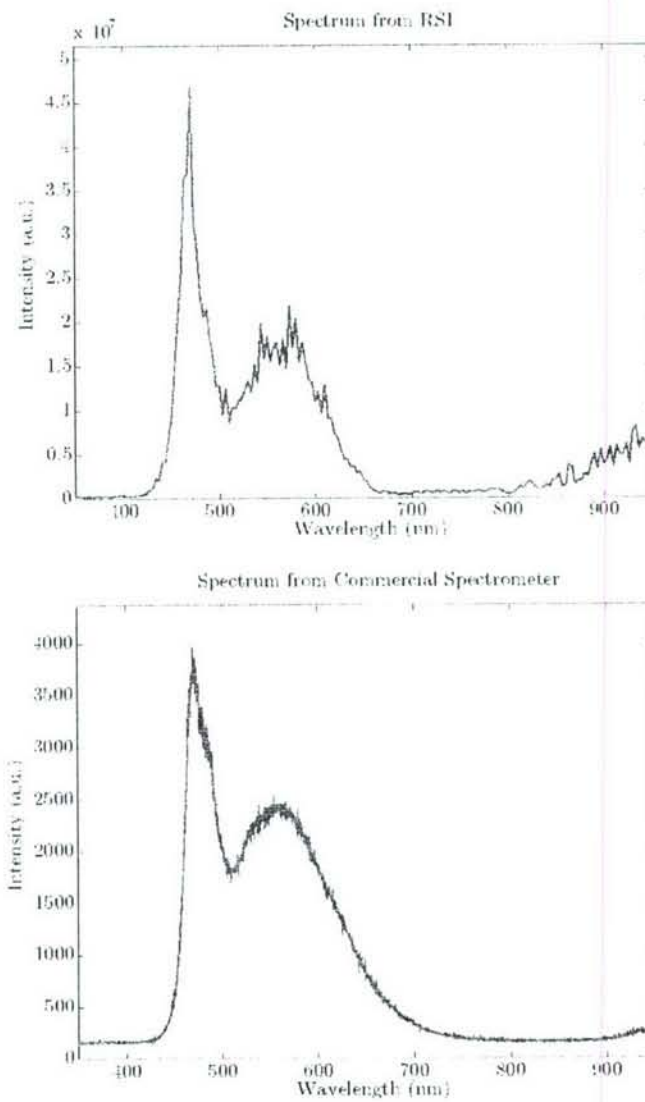
Figure 2.11: White LED spectrum measured by RSI (top) and measured by a commercial spectrometer (bottom)
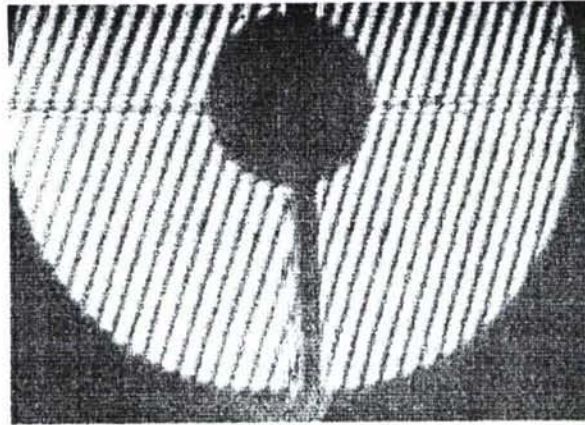
Figure 2.12: Obstruction in aperture caused by secondary mirror of telescope.
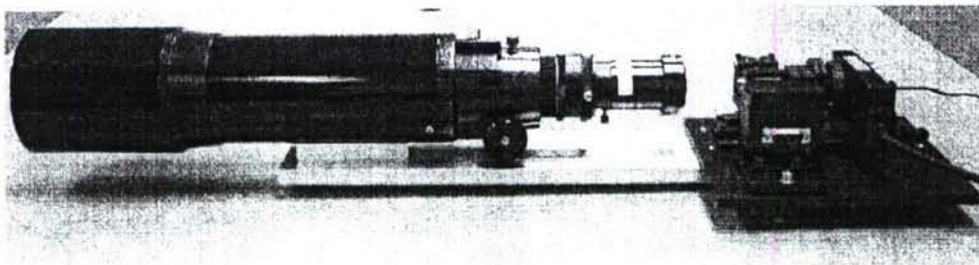

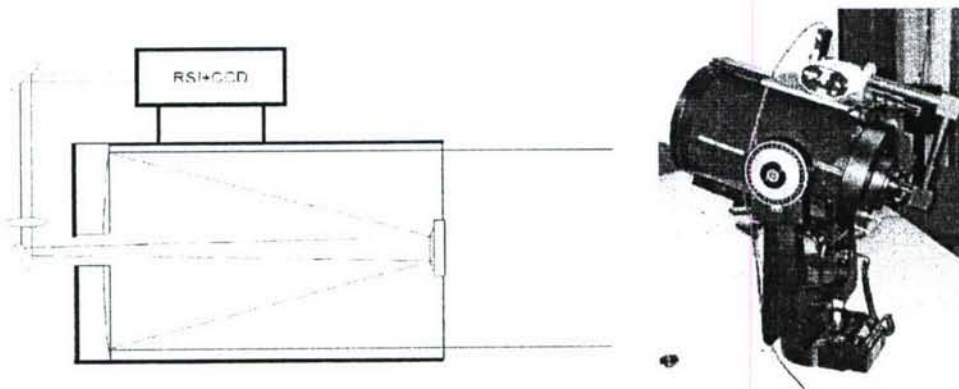Figure 2.13: RSI coupled to a 102 mm refracting telescope.

Figure 2.14: Diagram of RSI attached to SCT telescope (left), picture of RSI and SCT telescope system (right).
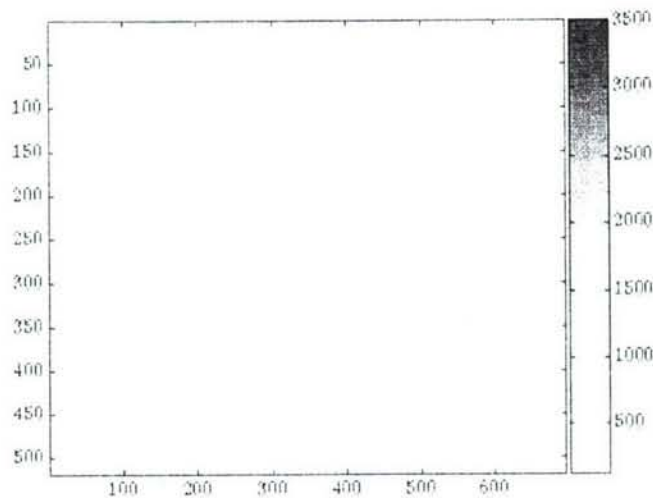
Figure 2.15: Fringe pattern recorded for the star Vega.

observation. Fringes were visible for integration times as low as 50 msec, but their poor signal-to-noise ratio made them difficult to analyze. An FFT of the fringe pattern from Fig. 2.15 and radial cross section of spectral information are shown in Fig. 2.16. There was a large amount of low frequency noise present in the fringe pattern, so a large area was deleted from the middle of the FFT image. The spectral resolution of the result is on the order of 10 nm per pixel.

A.4 Conclusions

The RSI / telescope system works as a proof-of-concept demonstration for interferometric spatio-spectral tracking. As can be seen in Fig 2.16, there are blurring problems that degrade the spectral data. This blurring is primarily caused by the shifting of the apparent location of the point source while acquiring a single frame. The two major causes of location shifting are inaccuracies in the telescope's tracking mount and atmospheric turbulence. A more stable telescope mount would produce
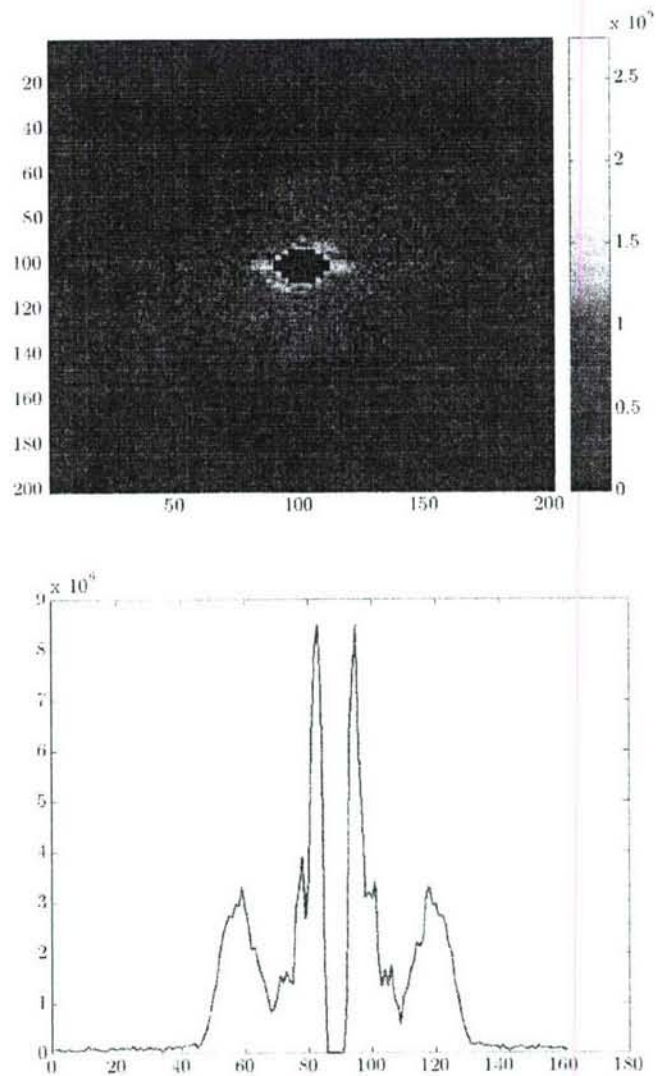
Figure 2.16: FFT of Vega fringes top) and cross section through spectral informa-
tion (bottom)

more accurate results. The effects of atmospheric turbulence can also be reduced by using a
procedure like that described in [10] and [11]. Rather than using long integration times on the
CCD to record a fringe pattern, sets of short exposure images can be recorded. These images are
then analyzed and corrected for spatial shifts of the source, and then summed together for a
higher quality image.

A - REFERENCE

A-1.   M. O. Harwitt and N. J. A. Sloane, *Hadamard Transform Optics*. New York: Academic Press, 1979.

A-2.   E. E. Fenimore and T. M. Cannon, "Coded aperture imaging with uniformly redundant arrays," *Applied Optics*, vol. 17, pp. 337–347, February 1978.

A-3.   S. R. Gottesman and E. E. Fenimore, "New family of binary arrays for coded aperture imaging," *Applied Optics*, vol. 28, pp. 4434–4352, October 1989.

A-4.   E. Caroli, J. B. Stephen, G. D. Cocco, L. Natalucci, and A. Spizzichino, "Coded aperture imaging in x-and gamma-ray astronomy," *Space Science Reviews*, vol. 45, pp. 349–403, 1987.

A-5.   E. G. Steward, *Fourier Optics An Introduction*. Mineola, NY: Dover Publications Inc., 2 ed., 2004.

A-6.   J. Strong and G. A. Vanasse, "Interferometrifc spectroscopy in the far infrared," *Journal of the Optical Society of America*, vol. 49, pp. 844–850, September 1959.

A-7.   L. Mertz, *Transformations in Optics*. New York: John Wiley & Sons, Inc., 1965.

A-8.   B. E. A. Saleh and M. C. Teich, *Fundamentals of Photonics*. New York: John Wiley & Sons, Inc., 1991.

A-9.   L. Mandel and E. Wolf, *Optical Coherence and Quantum Optics*. New York: Cambridge University Press, 1995.

A-10.   J. B. Breckinridge, "Coherence interferometer and astronomical applications," *Applied Optics*, vol. 11, pp. 2996–2998, Dec 1972.

A-11.   C. Roddier and F. Roddier, "High angular resolution observations of alpha orionis with a rotation shear interferometer," *Astrophysical Journal*, vol. 270, p. L23, 1983.

A-12.   C. Roddier and F. Roddier, "An image reconstruction of alpha orionis," *Astrophysical Journal*, vol. 295, p. L21, 1985.

A-13.   A. Chelli and J. M. Mariotti, "Visibility and phase analysis for image and pupil plane interferometry at optical wavelengths," *Astronomy and Astrophysics*, vol. 157, pp. 372–382, 1986.

A-14.   C. Roddier and F. Roddier, "Interferogram analysis using fourier transform techniques," *Applied Optics*, vol. 26, p. 1668, 1987.

A-15.   R. P. Korechoff, D. J. Diner, E. F. Tubbs, and S. L. Gaiser, "Extrasolar planet detection," *Astrophysics and Space Science*, vol. 212, pp. 369–383, 1994.

A-16.   T. Blake, "Modeling the aeos spectral imaging sensor (asis) for spectral image reconstruction," in *Proceedings of the Air Force Maui Optical and Super-computing Conference*, September 2005.

A-17.   A. Chaudhary, "Characterization of space aging of solar panels from non-resolved four-color photometry data," in *Proceedings of the Air Force Maui Optical and Supercomputing Conference*, September 2005.

A-18.   T. Payne, "Utility of a multi-color photometric signatures database," in *Proceedings of the Air Force Maui Optical and Supercomputing Conference*, September 2005.

B. Dispersive Instruments for Spatio-spectral Point Source Tracking

1. Introduction

Our previous work on spatio-spectral tracking has dealt with interferometric methods for simultaneously gathering spatial information for tracking and spectral information for the identification of nonresolved objects in orbit. Our interferometric system uses either a single or multiple rotational shear interferometers (RSIs). Computing the position and spectrum of a target point source requires two measurements with the RSI, either in sequence with a single RSI or simultaneously with an array of RSIs in parallel.

The fringe response of an RSI, as shown in Figure 1 encodes the target's spatial information in the orientation and frequency of the fringe pattern. The spectrum of the target is encoded in the intensity modulation pattern present in the fringes. The RSI-based system collects full spectral and tracking information in two measurements. This compares favorably with a typical instrument used in satellite tracking and astronomy: a four-color photometry system using BVRI filters. The four-color photometry system makes a measurement of the target with each of four filters, providing spatial information and spectral information averaged into four bands. The multiplex advantage that allows the RSI system to capture full spectral information in two measurements, however, exhibits the multiplex disadvantage in signal-to-noise ratio.
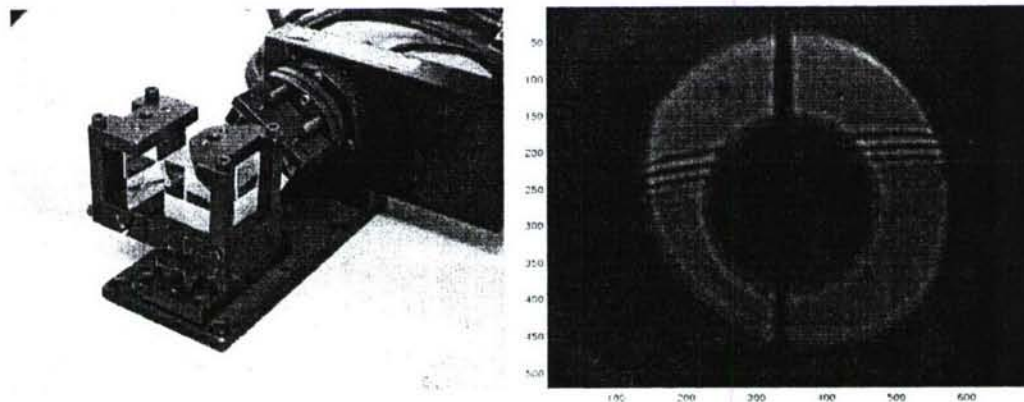

Figure 1. Photograph of a rotational shear interferometer (right) and fringe response recorded from a star (left).

Here we describe several instruments we have developed based on spectrally dispersive elements rather than interferometric designs. These systems also capture spatial and spectral information from a target point source, but do not exhibit the multiplex disadvantage in SNR. These systems concentrate the signal photons onto one or a few narrow bands on the detector, rather than the RSI, which distributes the signal photons across the entire detector. These dispersive systems are also less sensitive to vibration and precise alignment versus the RSI system. The first system is a simple proof-of-concept system that images the output of a telescope through a grating. The second system uses a custom designed multiplex holographic grating element to create a spatiospectral signature from a point source. The third system provides a spatio-spectral measurement with a set of three custom designed gratings.

B.2. Imaging Through A Grating

This spatio-spectral sensor is rather minimal, composed of a transmission grating and a digital focal plane. The system is designed to focus the telescope's image plane onto the focal plane through the grating. The system, shown in Figure 2, is built with a 90 degree geometry between the telescope output and CCD.

Figure 2. Diagram of a simple dispersive spatio-spectral tracking system.

The grating is placed in the middle, rotated 45 degrees from the telescope optical axis and 45 degrees from the normal of the CCD. The grating used in this design has a relatively high period of 2400 line pairs per millimeter, resulting in a spectral range of only 90nm (540 -630 nm). The grating is housed in a photopolymer housing printed on a rapid-prototyping system, designed to replace the eyepiece of a consumer grate telescope. The data recorded by the CCD is a single spectral stripe across the axis of the CCD that matches the dispersion axis of the grating. The location of this stripe along the *non*-dispersion axis of the CCD provides spatial information, locating the point source in the field of view of the telescope in one dimension. A second system can be used in parallel with the first, with dispersion axis rotated 90 degrees with respect to the first, to achieve two dimensional tracking information (elevation and azimuth angles). A photograph of the system and of the system's response to a point source is shown in Figure 3.
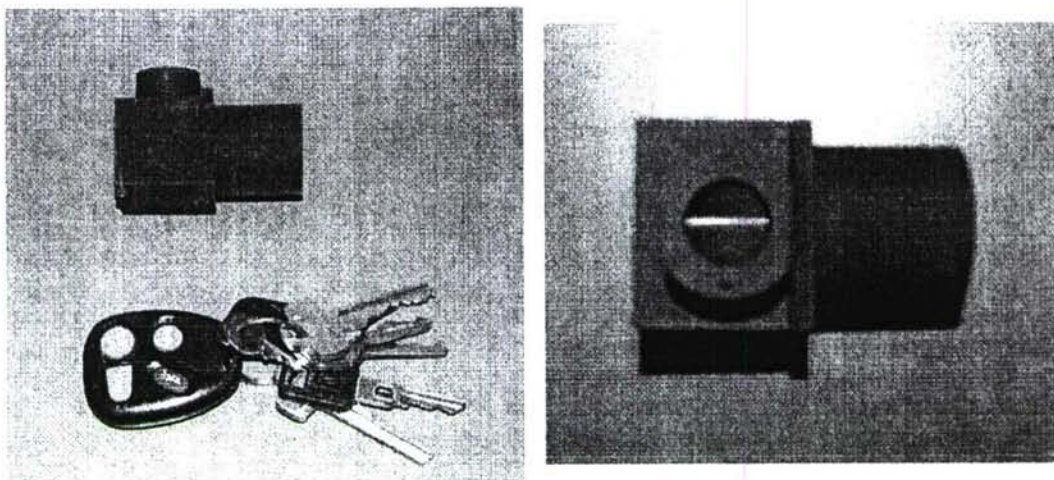
Figure 3. Photograph of the simple dispersive system and example of its response to a point source.

The spectral range shown in Fig. 3 is larger than the 90nm range of the instrument because the camera used for the photograph is capable of capturing a wider angle from the grating than the CCD used on the instrument. The spectral response of the point source is simply the intensity as recorded across the spectral stripe.

B.3. Dispersion Multiplexing With A Multiplex Transmission Hologram

The key feature of our second dispersive spatio-spectral sensor is a custom designed and fabricated multiplex holographic element. The hologram is designed to capture both spatial and spectral information of a point source in the telescope's field of view. The hologram contains three different grating periods, each at different rotation angles. The different grating periods target separate, but overlapping regions of the visible spectrum. The rotation angle of the holograms provides spatial information, relating the location of the point source within the field of view of the telescope. The system also images the 0th order diffraction from the holograms, which can also be used to spatially track the source.

The hologram has three different grating periods recorded on it, rotated with respect to each other. One grating period disperses its spectrum across the horizontal dimension of the CCD, and the other two disperse their spectra at a rotation angle of (+ and -)19.61 degrees from the horizontal – along the diagonals of the CCD. Fig. 4 shows the calculated response of the holographic element. The system records the 0 and +1 order diffraction from the hologram, as shown by the shaded region in Fig. 4 representing the CCD. The specifications for the three spectral bands are listed in Table B.1.

Ali Adibi's research group at Georgia Tech fabricated the holographic elements specified for both of the dispersion multiplexing systems in this paper.
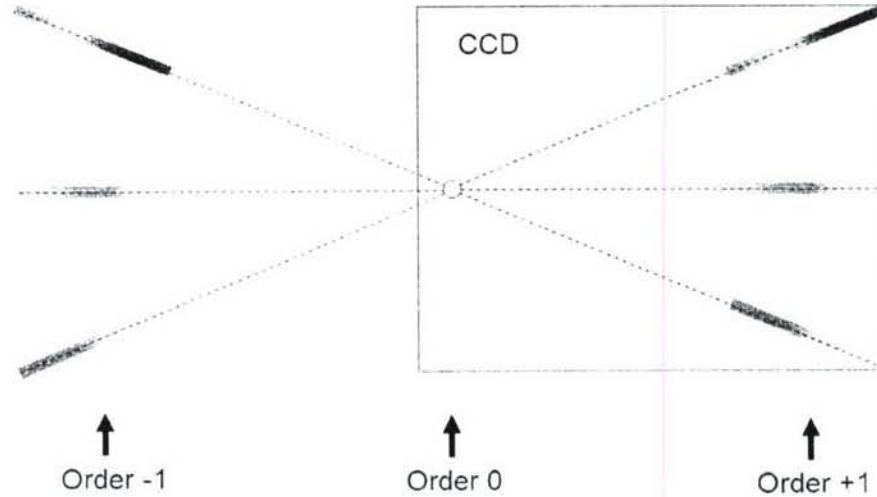
Figure 4. Calculated response for the second system's multiplex hologram.

	Grating 1	Grating 2	Grating 3
Center Wavelength (nm)	475	600	725
Spectral Bandwidth (nm)	450 - 500	525 - 675	650 - 800
Grating Period (lines per micron)	0.374	0.275	0.257
Estimated Spectral Resolution (nm per pixel)	0.96	0.94	1.0

Table B.1. Spectral Band Data

A diagram of the optical system for this spatio-spectral sensor is shown in Figure 5. The lenses in the system all have a diameter of 25mm. The hologram is 15 mm in diameter. One of the key features in this design is that the CCD is not centered on the optical axis of the rest of the optical system. It is shifted 3 mm "right", along the longer dimension of the CCD. This is depicted in Figure 4. This system is also built using a photopolymer structer printed on a rapid prototyping machine. After the optics are assembled in the polymer structure, the structure is attached to a cooled CCD camera with a resolution of 765 x 510 pixels. During testing, we operated the camera at 0 degrees C. The system is shown in Figure 6, both by itself and attached to a telescope. The telescope used to track and collect light from the target is a Schmidt-Cassegrain style telescope with a 254 mm aperture and f/6.3 optics. The hologram described in this section proved to be quite challenging to manufacture. The hologram used in the constructed system is similar to the calculated specifications, except that the dispersion pattern is magnified and the spectral ranges of the bands are extended. The dispersion pattern is magnified such that only two of the spectral bands can be resolved on the CCD at once. The angle between any two of the three spectral bands is sufficient to locate the target point source by calculating the position where the two lines intersect. This intersection is usually located beyond the visibility range of the CCD, but with the CCD pixel size and specifications for the telescope optics we can

easily calculate the location of the target. Since the spectral range of the bands has been extended, one of the diagonal bands measures approximately 450nm of bandwidth, from $450 - 900nm$.
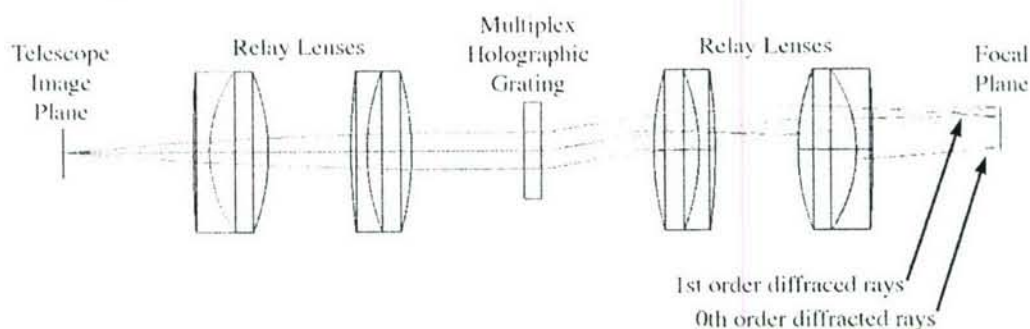

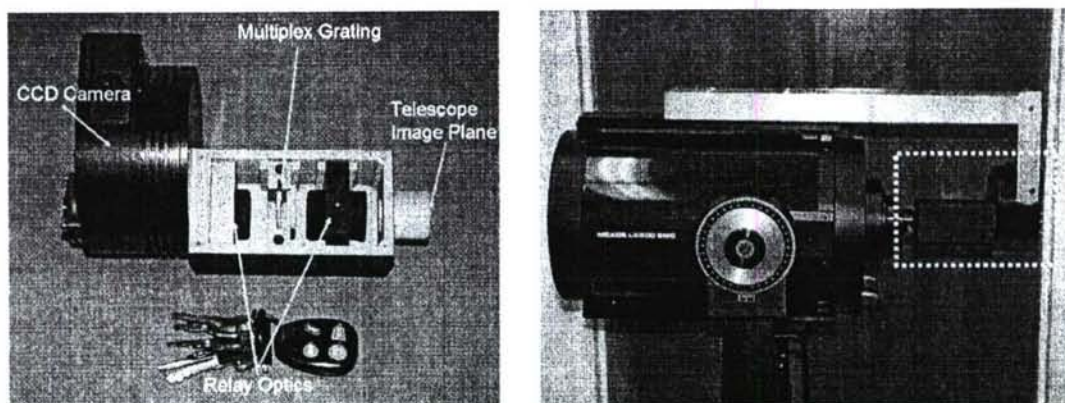Figure 5. Diagram of optical components for second system.

Figure 6. Photograph of second spatio-spectral tracking system. The sysem is shown opened, on the left, and attached to a telescope, on the right.

Figure 7 shows two datasets taken with this spatio-spectral tracking system. The first dataset shows the CCD measurement of a krypton pen lamp and the spectrum calculated for the pen lamp. The second dataset shows the measurement recorded for Polaris, and the corresponding spectrum.
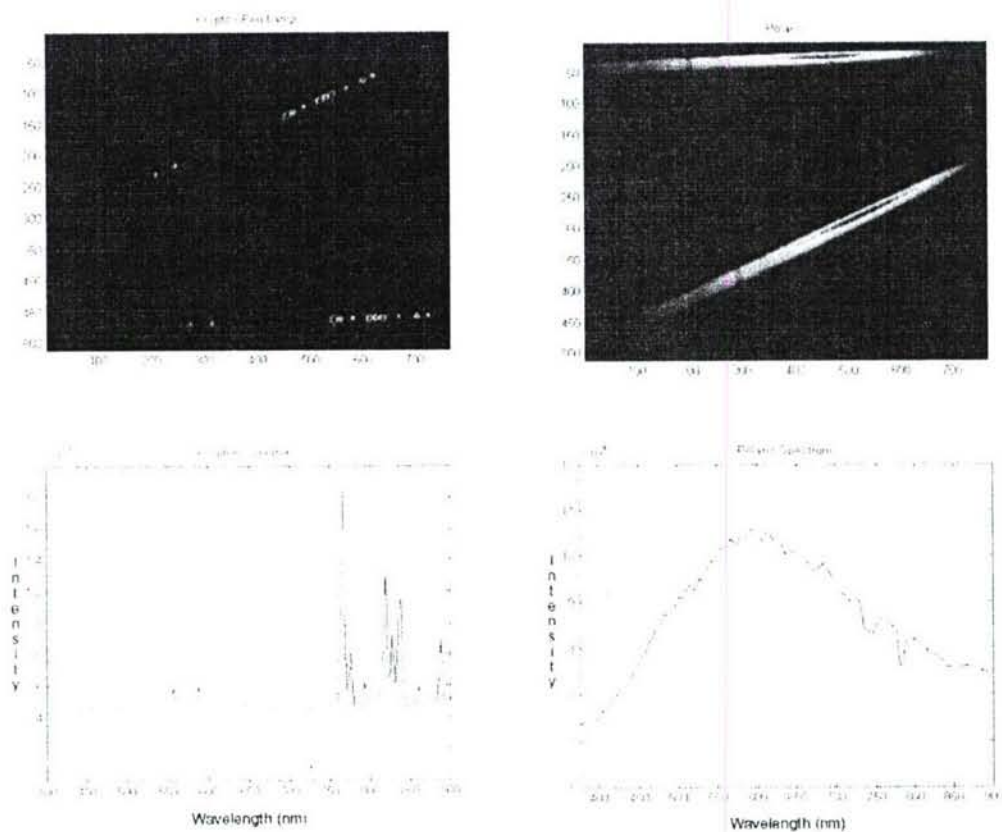
Figure 7. Experimental data for the second system. The first column shows the response to a krypton pen lamp (above) and the spectrum of the penlamp (below). The second column shows similar data for the star, Polaris.

B.4. Dispersion Multiplexing With A Set of Gratings

The third dispersion-based system we developed for spatio-spectral tracking, like the second, uses dispersion multiplexing. Rather than implementing a multiplex dispersion pattern with a single hologram, this system uses a set of three separate gratings. Each grating is recorded on its own substrate with a specific grating period and corresponding spectral response range. When the gratings are installed in the system, they are rotated at a fixed angle with respect to each other. The rotation angle between the gratings produces the spatial information used to track the target point source. The expected system response to a point source measured by the detector is shown in Figure 8. Table B.2 describes the spectral response for the three holograms
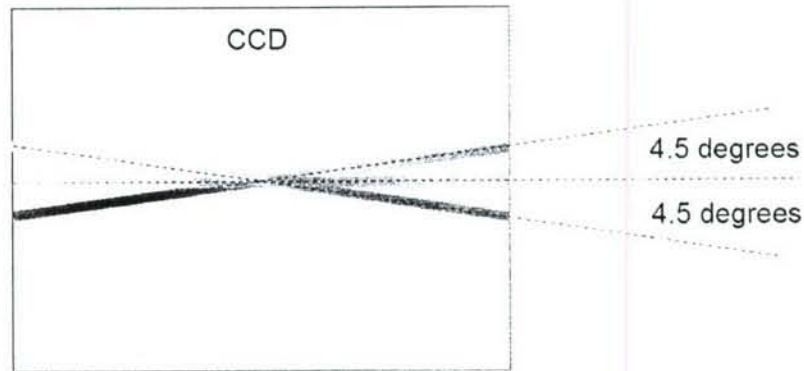
Figure 8. Calculated point source response for System 3.

	Hologram 1	Hologram 2	Hologram 3
Center Wavelength (nm)	452	530	634
1/e Spectral Bandwidth (nm)	376 -530	424 -646	474 -804

Table B.2. Spectral data for holograms in system three.

As noted by the color in Figure 8 and the specifications in Table 2, each grating period covers a separate, but overlapping, segment of the spectrum. This device should be sensitive from 400-750 nm with a spectral resolution better than 1 nm. The intersection between the three spectral bands on the CCD indicates the location of the target. The azimuth and elevation angle to the target can be calculated given the pixel number of the intersection and knowledge of the telescope's optics.

This system also uses 25mm optics and the same cooled 764x510 resolution camera as described in the previous section. It is also designed for use with our 254mm diameter f/6.3 Schmidt-Cassegrain telescope. Figure 9 shows the diagram for the optical system
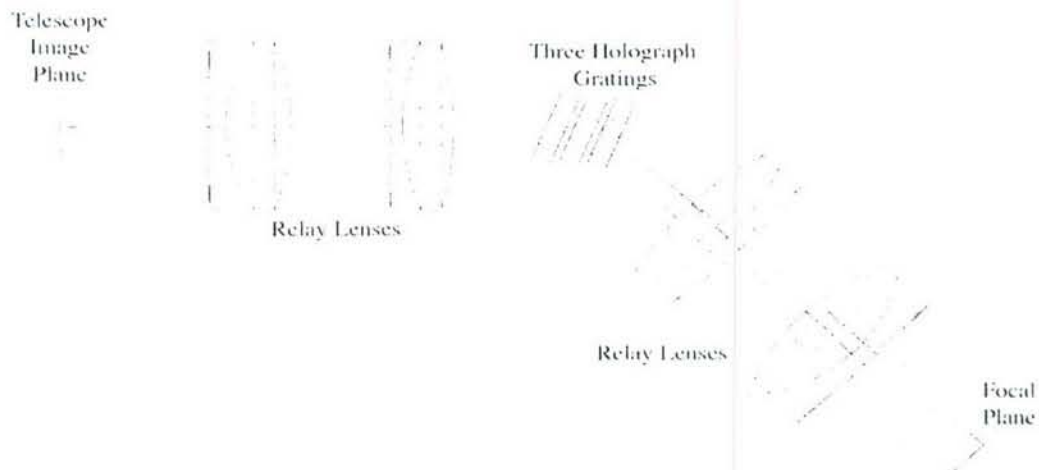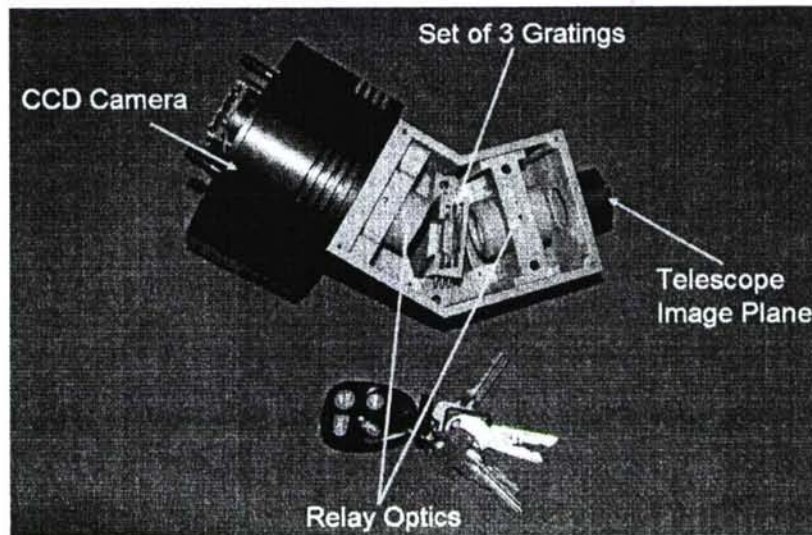

Figure 9. Diagram of optical components for third system.

The assembled prototype is shown in Figure 10.

Set of 3 Gratings
CCD Camera
Telescope Image Plane
Relay Optics

B.5. Summary

A three telescope-coupled spatio-spectral tracking systems based on spectrally dispersive elements has been described. These systems have both improved mechanical stability and signal-to-noise ratio versus an interferometric system. Two of these systems can capture two dimensions of tracking data and 400nm of spectral bandwidth (visible through NIR) in a single measurement. While these systems can be further optimized for increased spectral resolution and spectral bandwidth, they present a good solution for spatio-spectral point source tracking.

C. Dispersion Multiplexing Spectrometer

Current environmental sensing, defense and research applications demand compact and inexpensive spectrometers that maintain a high level of performance. This chapter describes a spectrometer to meet this goal by using aperture coding and dispersion multiplexing with broadband filtering.

A traditional dispersive spectrometer is composed of three primary elements: an input aperture, a digital focal plane, and a dispersive element. Other optics are usually present, optimized to relay light between the primary elements while minimizing optical aberrations. This spectrometer is operated under the assumption that uniform, spatially incoherent light fully fills the aperture. In order to achieve reasonable spectral resolution, this requires the aperture to be a spatial filter (typically a slit) to limit the angular extent of the source input to the spectrometer. When examining a diffuse source the slit blocks the majority of the photons incident on the instrument, limiting light throughput to the spectrometer. This is one of the major trade-offs in slit-based dispersion spectrometer design: spectral resolution versus light throughput. Increasing light throughput in a slit spectrometer while maintaining spectral resolution requires a taller slit and detector, effectively increasing the size and cost of the

system. One solution to this problem is to replace the slit with a coded mask with many times the open area of a single slit.

The most expensive single part of a dispersion spectrometer is typically the detector array. The primary reason for this is the demand for spectrometers with the sensitivity to measure low-intensity samples. This challenge is exacerbated by the resolution-throughput trade-off in a slit-based device. A secondary reason for the high cost of spectroscopy detector arrays is their non-standard aspect ratio. Detector arrays produced in high volume typically use an aspect ratio of 4:3 or 16:9, to be used in consumer imaging devices. Many spectrometers use a non-commodity detector with an aspect ratio of 4:1 or more to increase the number of detector elements along the dispersion axis, thereby increasing spectral resolution. Dispersion multiplexing allows us to use a standard aspect-ratio focal plane by overlaying several spectral ranges across the dispersion axis of the detector. One commercial system uses a form of dispersion multiplexing by dispersing two spectral ranges along discrete stripes, separated along the non-dispersion axis of the CCD [C-1]. (They do, however, use a standard spectroscopy detector array.) Our technique uses a transmissive holographic grating with multiple grating periods recorded in it to disperse three spectral ranges across the entire extent of the detector.

This section describes a doubly multiplexed spectrometer, using both aperture coding and dispersion multiplexing. This system is a computational sensor that measures a combination of components of the input spectrum at each pixel location which can be processed to provide a spectral measurement. This chapter discusses the design and implementation of this dispersion multiplexing spectrometer. The key concept introduced is dispersion multiplexing with broadband filtering. The theory of and computational inversion algorithm required by dispersion multiplexing are described, as well as the details of our miniature implementation.

C.1 Coded Aperture Spectroscopy

Replacing the slit used in the aperture of a traditional dispersion-based spectrometer with a two-dimensional coded aperture with many openings allows us to overcome the trade-off between spectral resolution and light throughput faced by spectrometer designers. This is particularly advantageous for systems used to measure the spectra of diffuse sources, since the constant radiance theorem states that light from a diffuse, incoherent source cannot be focused or have its intensity increased through (de)magnification [C-2]. Other techniques used in spectroscopic instruments to overcome the resolution-throughput trade-off include the use of a structured fiber bundle for light collection or interferometric-based (non-dispersive) techniques [C-3, C-4]. Neither of these techniques are useful for a low cost spectrometer. The fiber bundle can collect light over a large aperture on one end, but on the other, the bundle must be stacked to imitate the shape of a slit, requiring large optics and detector for a large collection area. The design stability and tolerances for interferometric spectrometers make them prohibitively expensive when compared to a dispersion-based device.

Coded aperture spectrometers, introduced as multi-slit spectrometers, were initially implemented with single channel detectors and moving masks. [31–33] These devices were used to increase light throughput without loss of spectral resolution. Eventually an entire class of

spectrometer was developed, known as the Hadamard Transform Spectrometer (HTS). [A-1] The basis for the HTS was a moving mask (or set of masks) with a series of openings based on the Hadamard matrix. The primary disadvantage of the HTS systems using a single channel detector is the time required to take the measurement—each spectral measurement requires a full set of detector measurements for each position of the moveable mask. Since multichannel detectors have become widely available, coded aperture spectrometers have been implemented with spatial light modulators (SLM) and micro-electromechanical mirror (MEM) arrays to simulate the moving masks [C-9, C-10]. With a two-dimensional aperture code and a two-dimensional array detector, it is possible to measure the spectrum with single shot. Our design uses a static coded aperture made of a two-dimensional chrome pattern deposited on glass, a simpler and more cost effective solution than the MEM and SLM based designs. Below we discuss the theory behind our coding scheme. A more detailed discussion can be found in a prior publication [C-11].
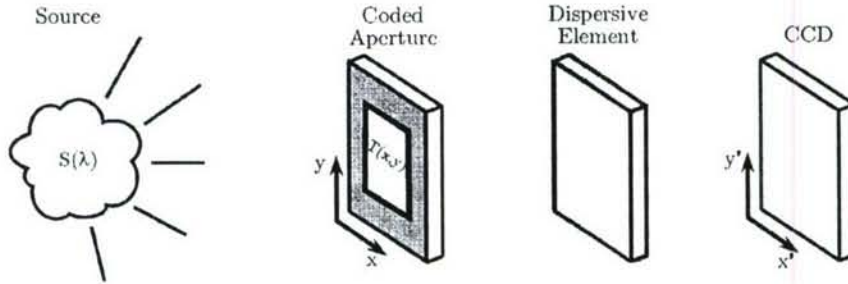

Figure 4.1: Diagram of a traditional dispersive spectrometer.

Figure 4.1 shows a simple schematic of a coded aperture spectrometer and defines the coordinate systems used in this section. Light incident on the detector plane can be represented by Eq. 4.1.

$$I(x',y') = \iiint \delta\big(x-(x'+\alpha(\lambda-\lambda_{c\pi}))\big)\delta(y-y')T(x,y)S(x,y;\lambda)dxdyd\lambda \quad (C.1)$$

Here $\delta\big(x-(x'+\alpha(\lambda-\lambda_{c\pi}))\big)$ is the propagation kernel for a dispersive spectrometer with no internal magnification and with linear dispersion of α along the x axis and center wavelength of λ_c at $x = 0$ for all y. $T(x,y)$ represents the transmittance function of a two-dimensional aperture mask, and $S(x,y;\lambda)$ represents the spectral density as a function of position in the aperture. Since this paper focuses on a spectrometer and not a hyperspectral imager, we assume that there is no

spatial structure in the input spectrum of the aperture. This means that $S(x,y;\lambda)$ is constant in x and y, reducing the spectral density to $S(\lambda)$. This reduces Eq. C.1 to

$$I(x',y') = \int T(x,y')S\left(\lambda = \frac{x-x'}{\alpha} + \lambda_c\right)dx . \text{(C.2)}$$

This means that the intensity measured at the detector is a one-dimensional convolution between the spectrum of the source and the transmittance function of the aperture, measured along the dispersion axis of the detector. For a slit-based dispersive spectrometer with the slit at $x = x_o$, $T(x,y)$ can be approximated by a delta function, $\delta(x-x_o)$, so that one position in x' on the detector corresponds to the intensity at a single wavelength:

$$I(x',y') = S\left(\lambda = \frac{x_0 - x'}{\alpha} + \lambda_c\right) \text{(C.3)}$$

Using a coded transmittance pattern for $T(x,y)$ causes the instrument to become a multiplex device such that one position on the detector in (x,y) measures the sum of the intensities at several wavelengths. This $T(x,y)$ must be properly designed to yield an accurate estimation of the source spectrum.

Previously we have shown that mask transmittance patterns based on families of orthogonal functions are suffcient for the design requirements of a system based on a coded aperture mask. [C-11] Traditionally, the Hadamard matrix has been used as the basis for coded aperture spectrometers. The order-p Hadamard matrix is an orthogonal matrix with p rows, originally derived as an optimal solution for making a multiplex measure of several weights in the presence of noise. [A-1,C-12] A mask based on an order-12 Hadamard matrix is shown in Fig. 4.2. While the order-12 Hadamard matrix has 12 rows, this mask has been constructed according to a previously published row doubling procedure, yielding the 24 rows shown in the figure. [C-11]

In a dispersive spectrometer, a coded aperture system decouples spectral resolution from light throughput. For a traditional slit-based spectrometer, a required minimum spectral resolution specifies a maximum slit width, w. A system based on a coded aperture achieves the same spectral resolution by using a feature size of w, where feature size refers to the size of one of the open elements in the aperture mask. Since the coded aperture is constructed of a number of these open elements, it has a larger entrance aperture area and therefore higher light throughput versus the slit. For an aperture based on the order-p Hadamard matrix, there is a 50% loss of light because half of the mask features are opaque. This means that the Hadamard-code based system achieves $p/2$ times the light throughput of the traditional system when considering a diffuse source that fully fills the input aperture. Further, a finer-pitched mask pattern covering the same aperture area as the original pattern maintains the same light throughput, but increases the spectral resolution of the coded aperture spectrometer.
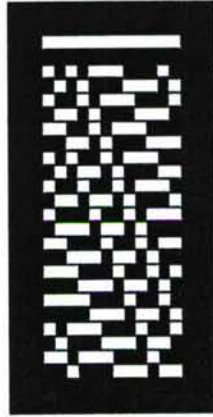
Figure 4.2: Diagram of a row-doubled Hadamard aperture mask based on an order-12 Hadamard matrix. White areas indicate light transmission, and black areas indicate where light is blocked.

To recover the target spectrum, we take the data from the detector, subtract a dark image to reduce the pattern noise and then slightly shift each row to correct for the "smile" distortion present in grating spectrometers. [22] The smile distortion can be easily characterized by looking at a target with distinct spectral features like a gas discharge lamp. It is also possible to reduce smile distortion by introducing a "negative" curvature to the aperture pattern when fabricating the mask, a technique currently used in some slit spectrometers. Generally, we design our aperture mask such that a single mask element covers several pixels on the detector. The last step before inversion is to average the set of pixel rows (along the non-dispersion axis of the spectrometer) that make up a single mask feature. The result for a mask with r rows is a set of r data vectors with length corresponding to the number of pixels along dispersion axis of the detector. A mathematical formulation of this is shown in the following equation, where the rows of M are the data vectors from the detector, the rows of W are spectral estimates formed for each row of input data, and H is the matrix representation of the aperture code.

$$\mathbf{H} \bullet \mathbf{W} = \mathbf{M} \quad (\text{C.4})$$

A non-negative least squares inversion algorithm is used to calculate the spectra in W .
(Typically we use the *lsqnonneg* function built into Matlab.) We then average these r spectral
estimates to determine the spectrum of the target.

C.2 Dispersion Multiplexing

In a traditional slit-based dispersion spectrometer the source spectrum is spread across the
detector. A one-dimensional detector is suffcient to record the entire spectrum, though a two-
dimensional detector is frequently used to increase SNR. For a fixed size detector and a target
spectral range, this traditional spectrometer system design is completely specified — the
maximum spectral resolution is set by the number of pixels on the detector along the dispersion
axis. (Aberrations in the relay optics and a slit width not optimized for maximum spectral
resolution can, however, reduce the spectral resolution.) To increase spectral resolution, one
must either decrease the spectral range of interest or replace the detector with a higher resolution
(and more expensive) model. Assuming the use of a two-dimensional detector, dispersion
multiplexing provides an alternative that can increase spectral resolution with the same detector
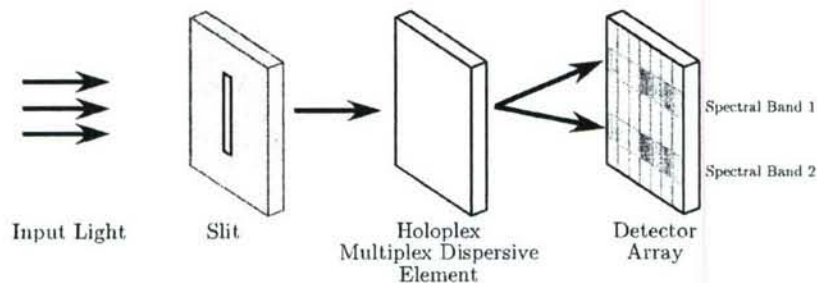and the same spectral range.

Figure 4.3: Diagram of the *Holoplex* multiplex holographic dispersive element.

Holographic gratings are useful for dispersion multiplexing spectrometers due to their
flexibility in implementing different dispersion patterns. One commercial system, the Kaiser
Holoplex, disperses two separate spectral bands on the detector, each covering a different
spectral range. [C-1, C-15] The spectral bands are separated along the non-dispersion axis of the
detector, as shown in Fig. 4.3. Our system uses a multiplex holographic grating with three

different grating periods. The Bragg wavelength selectivity of the hologram is tuned so that each of the gratings responds to a different spectral band, as shown in Fig. 4.4. The grating periods are set to disperse the spectral range of each band fully across the detector. This results in three spectral bands incident on the same detector pixels. To disambiguate these overlapping bands we use broadband filters that match the spectral range for each band. While it is possible to implement this type of dispersion multiplexing spectrometer with a set of disambiguation filters external to the detector, we chose to use a simpler and more cost effective color CCD.[†] This combines the broadband filters and detector into a single component. A typical color digital focal plane records data in three

[†]Another alternative is to use a focal plane whose pixels have some inherent spectral response. For example, the detectors made by *Foveon* detect the standard red, green, and blue color channels of a color CCD at each pixel location by using a special triple-well structure. This pixel structure effectively stacks a red-, green-, and blue-sensitive pixel vertically at each location. [C-19,C-20]
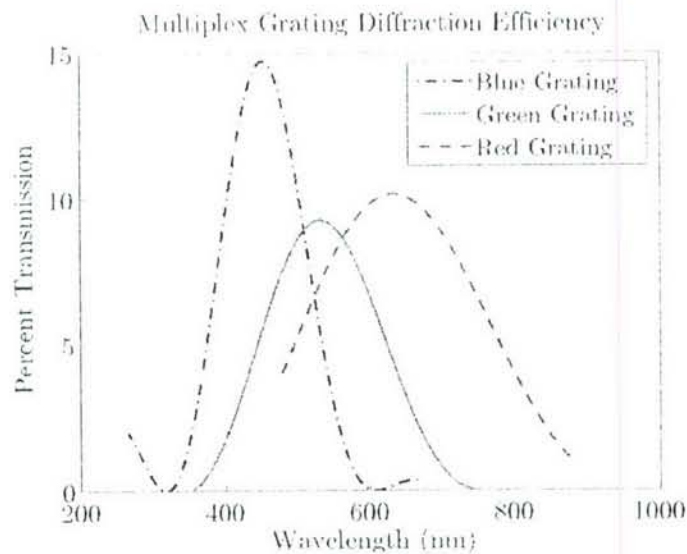

Figure 4.4: Spectral responses of each grating recorded in the hologram due to Bragg selectivity.

spectral bands by using an array of red, green, and blue (RGB) per-pixel filters. The standard

pattern of RGB filters used on a color focal plane is known as the Bayer pattern, as shown in Fig. 4.5. [C-16] This filter pattern provides one sample of green in each column of the detector and one sample of red and blue in alternating columns of the detector. For a detector with N pixels along the dispersion axis of the detector, this yields N samples of the green spectral band and $N/2$ samples for each of the red and blue spectral bands for our system.

The spectral responses of the Bayer pattern filters used in our system are shown in Fig. 4.6. These responses are typical of filters used in RGB color imaging. The red-filtered pixels provide an estimate of the spectrum within the red spectral band. Similarly, the green-and blue-filtered pixels estimate their respective spectral bands. As shown in Fig. 4.6, the RGB filter responses overlap. This causes the three spectral ranges sensed by our dispersion multiplexing spectrometer to overlap. It is necessary to correct for this overlap to eliminate spurious spectral features from our final spectral estimate.
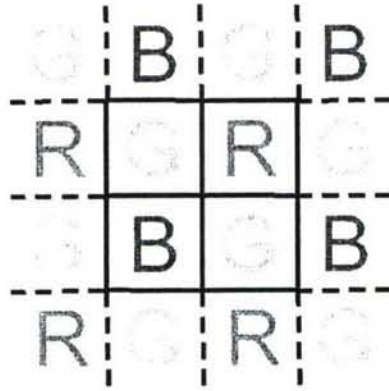

Figure 4.5: The Bayer filter pattern. Each square represents a pixel, and each letter represents either a red, green, or blue filter.

If we assume, in a traditional dispersion spectrometer, that the dispersion direction of the instrument corresponds to the horizontal axis of the detector, then each column of the detector represents a specific element of spectral resolution. A single column of the detector in our dispersion multiplexing spectrometer corresponds to three elements of spectral resolution – one for each of the spectral bands on the detector. Since the the per-pixel filter functions are smooth, we can label a column's spectral resolution elements for its center wavelength: λ, λ_r, and λ_b. In our system we treat every two columns on the detector as one column of output data, giving us one sample of red and blue and two of green for each element of spectral resolution. If we record the values (R, G, B) for one effective column of the detector, then we can calculate the proper values, accounting for overlap in the spectral bands, (r, g, b) by solving Eq. C.5. The $F_{color}(\lambda)$ represents the value of the R, G, or B filter functions at the wavelength corresponding to the